RSC Advances

PAPER

View Article Online
View Journal | View Issue

Cite this: *RSC Adv.*, 2021, **11**, 18440

Magnetic-gold theranostic nanoagent used for targeting quad modalities T_1 & T_2-MRI/CT/PA imaging and photothermal therapy of tumours†

Jinlei Liu,‡[a] Dan Wang‡[b] and Guannan Wang *[ac]

We describe a new type of ultra-small magneto-gold nanoparticle (MGN) with folic acid (FA)-based tumour targeting and multimodal imaging-guided photothermal therapy (PTT) properties that can be used as a theranostic nanoagent. The nanoagent integrates these MGNs–FA with surface modifications, and as expected, is monodisperse, and exhibits small size, strong NIR absorption, photothermal stability, good relaxivity and X-ray absorption coefficient, tumour targeting and excellent biocompatibility. Based on these properties, the nanoagent was successfully tested, both as a photothermal agent for high PTT efficacy and as a multimodality contrast agent for T_1- & T_2-MRI/CT/PA imaging *in vitro* and *in vivo*. Notably, the results of *in vivo* theranostic experiments with these MGNs–FA showed that they are highly effective and safe, indicating that they are efficient and promising theranostic agents that permit comprehensive imaging for diagnosis and therapy.

Received 15th March 2021
Accepted 8th May 2021

DOI: 10.1039/d1ra02041b

rsc.li/rsc-advances

Introduction

In the last few decades, theranostic platforms that can combine real-time multimodality diagnostic imaging and synergistic therapy have attracted enormous attention.[1–4] Multimodality imaging for diagnosis is achieved by combining two or more imaging modalities,[5,6] for example magnetic resonance imaging (MRI) and computed tomography (CT) are widely employed together for non-invasive imaging and diagnosis of cancer due to their properties such as excellent spatial resolution with 3D rendering function and high tissue penetration.[7] Nevertheless, CT and MRI suffer from low sensitivity when used for imaging early-stage tumours, compared to optical imaging modalities such as fluorescence imaging and photoacoustic imaging (PAI), which are capable of real-time dynamic imaging with high sensitivity and temporal resolution.[8] Notably, while conventional fluorescence imaging suffers from low tissue penetrance and cancer-to-normal tissue contrast,[9] PAI integrates optical excitation with ultrasonic detection, which substantially increases tissue penetrance to several centimetres while maintaining high temporal resolution in real-time, implying significant potential as a complementary approach to established imaging techniques.[6,8] Thus, a combination of MRI, CT and PAI can circumvent the limitations of these individual modalities to yield a more accurate diagnosis based on images with high spatial and temporal resolution. These characteristics can also provide insight, understanding and real-time assessment of cancer origin, morphology and invasiveness, which are crucial for cancer diagnosis and treatment.

In the last 50 years, despite the possibility of resection, the mainstays of clinical cancer therapy have remained chemotherapy and radiotherapy, but these approaches are limited by chemoresistance and non-selective cytotoxicity, which result in low therapeutic efficacy and serious side effects in patients. Further, radio-resistance and restrictions in radiation dosages can eventually lead to failure to treatment.[10] Importantly, due to factors such as absence of tumour targeting and damage to the immune system, these modalities cannot provide feedback that permits timely evaluation of the clinical effectiveness of treatment—the latter needs to be urgently addressed as it is also the main reason why personalised cancer treatment is hard to achieve.[11] NIR-based photothermal therapy (PTT) is an advanced method that has shown considerable promise in cancer therapy[2,3,5,7,12] owing to properties such as minimal invasiveness, superior treatment efficacy, remote operation and few systemic side effects. It involves employing photothermal conversion agents (PTCAs) that generate heat for cancer cell ablation upon irradiation with a near-infrared (NIR) laser.

In light of rapid development of nanotechnology in biomedicine due to their unique physicochemical properties

[a]*The First Affiliated Hospital of Jinzhou Medical University, Jinzhou, 121001, China. E-mail: chemwangguannan@gmail.com; Fax: +86-537-7907618; Tel: +86-537-7907618*

[b]*Basic Medical College, Beihua University, Jilin City, 132013, China*

[c]*College of Biomedical Engineering & the Key Laboratory for Medical Functional Nanomaterials, Jining Medical University, Jining, 272067, China*

† Electronic supplementary information (ESI) available: Hemolysis assay of MGN–FA with various concentration incubation with red blood cells; flow cytometry measurement of cells after uptake of Cy5-labelled MGNs–FA and Cy5-labelled MGNs; the tumor volume change during 14 days of PTT therapy. See DOI: 10.1039/d1ra02041b

‡ These two authors contributed equally to this work.

and ease of functionalization, the emergence of nanoplatforms integrate several types of functional components for the fabrication of a smart "all-in-one" theranostics nanoplatforms to offer unprecedented possibilities in precision treatment of cancer,[13] including various nanomaterials of Fe_3O_4,[14] Gd_2O_3,[15] gold,[16] semiconductors[17] and transition-metals,[18] *et al.* Among these nanomaterials, magnetic nanoparticles are widely used as contrast agents (CA) in MRI due to their natural presence in the human body,[19] *e.g.* Resovist (ferucarbotran) and Feraheme (ferumoxytol) are two typically used, clinically approved, dextran-coated iron oxides.[20] Gold nanoparticles (AuNPs) are another class of nanoparticles that have attracted prominent research interest due to their outstanding biocompatibility, persistence in circulation, convenience for modification and potential applications in biomedicine.[7,10,16] Au-based nanomaterials are also used in CT imaging, surface-enhanced Raman spectroscopy imaging, and photoacoustic imaging (PAI).[5,10,16,21] Furthermore, AuNPs are an efficient system for photothermal conversion and can be used in PTT.[21,22] Therefore, magneto-gold nanoparticles (MGNs) that combine Au and magnetic nanoparticles are promising theranostic nanoagents that can be used for cancer therapy.

Given the versatile physicochemical properties of MGNs, recent preclinical studies have demonstrated their applications in multimodal imaging and tumour therapy wherein some of the limitations associated with individual approaches for cancer treatment were overcome. Specifically, Shi's group have taken the lead in synthesising a core–shell of Fe_3O_4@-hybrid@Au nanoparticles that serve as an efficient imaging agent for negative (T_2)-MRI and PTT.[23] In another study, Zhang *et al.* have described the synthesis of γ-Fe_2O_3@Au nanoflowers for *in vivo* PAI, T_2-MRI and SERS imaging.[24] Lu and colleagues have prepared polypyrrole-coated Fe_3O_4/Au nanocomposites based on gold and Fe_3O_4 nanoparticles using the assembling method for potential application in *in vivo* T_2-MRI/CT guided PTT.[2] We have recently described a new type of biocompatible ultra-small magnetic-gold (Fe_3O_4–Au) nanoparticle that incorporates modifications such as fluorescence polymers and tumour-homing proteins. Notably, these nanoparticles permit simultaneous *in vivo* tumour targeting, positive (T_1)- & negative (T_2)-weighted MRI/CT/fluorescence multimodality imaging and chemosensitisation.[4] Although preclinical studies have reported that MGNs are promising agents for the development of cancer theranostics due to their versatile physicochemical properties, MGNs are large and complex structures that require multi-step preparation and carry a risk of biotoxicity. To date, no attempts have been made to explore MGNs as tumour targeting theranostic nanoagents for T_1- & T_2-MRI/CT/PAI quad-modality imaging and PTT.

Therefore, building on our nanoparticle design, the present paper describes a novel nanoagent that permits synergistic and effective multifunctionality. Specifically, we have prepared novel MGNs with significant features, including biocompatibility, NIR absorption and excellent relaxivity and X-ray absorption coefficient. Based on these properties, the MGNs can be used as both photothermal agents for PTT and as multimodality CA for T_1- & T_2-MRI/CT/PA imaging. Furthermore, they can also be easily conjugated with molecules *via* thiolate bonding, and a biodegradable and biofunctionalised polymer of poly(ethylene glycol) containing folic acid (FA) on one end was used to enhance tumour targeting characteristics and biocompatibility of the nanoagent. Results from *in vitro* and *in vivo* experiments show that the final resulting nanoparticles (MGNs–FA) had high targeted tumour cell uptake and were amenable to long-term tracking for therapy. This multifunctional magneto-gold nanoagent represents a promising platform for achieving efficient and safe tumour theranostics.

Experimental

Materials

FA–PEG–SH (MW = 3400) is a commercial product from Nanocs (NY, USA), LDH test kits were purchased from the Nanjing Institute of Bioengineering, China, and the calcein-AM/PI staining kits were purchased from Shanghai Dongren Chemical Technology Co., Ltd., China. Other chemicals and solvents were purchased from Sigma-Aldrich unless indicated otherwise.

Synthesis of MGNs and MGNs–FA

MGNs were synthesised as described by us previously but with slight modifications.[4] The MGNs (Fe_3O_4–Au, MGNs) were prepared using a modified coprecipitation method previously reported by us.[4] Briefly, 5 mg of ultra-small Fe_3O_4 nanoparticle cores were first synthesised and the MGNs were formed by the reduction of 3 mL of 2 mg mL^{-1} $HAuCl_4$ onto the surfaces of Fe_3O_4 with poly(acrylic acid) as the seeding agent and 0.5 mL of ice-cold $NaBH_4$ as the reducing agent at low temperature with constant mechanical stirring for 1 h. Dense MGNs were separated from the reaction solution by centrifugation and dispersed in tetrahydrofuran (THF). The centrifugation and redispersion steps were repeated thrice to remove unreacted ultra-small iron oxide. Next, thiol-terminated polymer (SH–PEG–FA, 100 μL, 10 mM) was added to the MGNs solution (2 mL, 25 nM) with gentle shaking, the mixture stirred at room temperature for at least 12 h. Finally, the obtained MGNs–FA were centrifugally separated and washed with water three times to remove the excess reagents, and purified by Sephacryl HR-300 gel medium. Purified MGNs–FA were redispersed in PBS solution (pH 7.4) as stock solution for future use.

Characterization

To characterise the hydrodynamic diameter of the synthesized nanoparticles dynamic light scattering (DLS) was determined using the Anton Paar Litesizer 500. UV-visible-NIR spectra were received by a Shimadzu UV-3600 spectrophotometer (Shimadzu Co., Japan). Transmission electron microscopy (TEM) was performed on an FEI TECNAI G20 high-resolution transmission electron microscope operating at 200 kV.

In vitro cytotoxicity

The MTT assay and the lactate dehydrogenase (LDH) leakage assay were used to evaluate *in vitro* cytotoxicity of the synthesised MGNs–FA. Cell viability was tested using the standard

MTT assay and activity of LDH in the culture medium was assessed using test kits wherein cells treated with hydrogen peroxide (H_2O_2) were used as positive control. Human umbilical vein endothelial cells (HUVEC) were cultured in RPMI-1640 medium (Gibco) with 10% (v/v) fetal bovine serum (Gibco), penicillin and streptomycin, at 37 °C under a 5% (v/v) CO_2 atmosphere. Cell density was determined using a haemocytometer. After confluence, cells were exposed to MGNs–FA or MGNs at various concentrations (500, 200, 100, 50, and 25 μg mL^{-1}) for 24 hours, and cells incubated without nanoparticles were used as controls. All procedures were carried out strictly in accordance with manufacturer's instructions and all experiments were performed in triplicate.

The hemolysis assay was also performed to test the damage to red blood cells. The red blood cells of mouse were obtained, then the 0.5 mL cells suspension was mixed with 1 mL of MGNs–FA nanoparticle PBS solution with various concentrations of 25, 50, 100, 200 and 500 μg mL^{-1}. The mixtures were then vortexed for 2 h at room temperature. The samples were centrifuged and the absorbance spectrum of the supernatants was measured by UV-Vis characterization. 1 mL of PBS and deionized water were used as negative control and positive control.

Evaluation of tumour targeting *in vitro*

Fluorescent cyanine (Cy5–PEG–SH) was used to track MGNs–FA to evaluate their tumour targeting capability. A mixture of FA–PEG–SH and fluorescent Cy5–PEG–SH (ratio of 9 : 1), was used to functionalise the surface of the MGNs to form Cy5-labelled MGNs–FA. Both human hepatoma cells (SMMC-7721) and HUVEC were used and an Olympus-FluoView FV10 confocal laser scanning microscope (CLSM) was used to image the cells treated with these nanoparticles. To measure the cell uptake of MGNs–FA, cells were incubated with Cy5-labelled MGNs–FA or Cy5-labelled MGNs (100 μg mL^{-1}) for one hour, washed with a large amount of PBS to remove any nanoparticles attached to the cell membrane, stained with DAPI (10 μg mL^{-1}) for 20 min, rinsed with PBS at least thrice, and imaged on a CLSM to evaluate cell morphology and locate nanoparticles within the cells.

Photothermal characteristics of MGNs–FA

The photothermal effect of MGNs–FA was measured in aqueous solution. Briefly, MGNs–FA (in 1 mL, at various concentrations of 500, 200, 100, 50, and 25 μg mL^{-1}) were exposed to an 808 nm NIR laser (power density: 1.0 W cm^{-2}) for 10 min, and the temperature was recorded.

Next, calcein-AM/PI staining was utilised to evaluate tumour cell-killing ability, which was defined as the readout for the photothermal effect. SMMC-7721 cells were pre-seeded into dishes and incubated with different formulations (PBS or 100 μg mL^{-1} MGNs–FA) for 12 h, followed by no exposure or treatment with NIR laser-based irradiation. Then, cells were mixed with calcein-AM/PI reagent, incubated at 37 °C for 15 min, and imaged under a fluorescence microscope (Olympus IX-73) to assess live and dead cell staining.

In vivo multimodality imaging

All animal procedures were performed in accordance with the Guidelines for Care and Use of Laboratory Animals of Jinzhou Medical University and approved by the Animal Ethics Committee of Jinzhou Medical University. A nude mouse xenograft model of SMMC-7721 human hepatocarcinoma cells was replicated according to a previously described protocol.

Mice were anaesthetised using 10% chloral hydrate and MGNs–FA dispersion solution (5 mg kg^{-1}) was intravenously administered through the tail vein. To demonstrate targeted accumulation of MGNs–FA for *in vivo* multimodal imaging, tumour-bearing mice were scanned 12 h after administration of MGNs–FA. For *in vivo* imaging, a 256-row, 512-slice spiral CT scan (Philips, Germany) was utilised and the imaging parameters were as follows: slice thickness, 0.625 mm; tube voltage, 100 kVp; and tube current, 100 mA. Raw data were reconstructed using 3D-Med software to acquire CT images and calculate CT values and CT data were analysed based on Hounsfield units (HUs) for regions of interest.

T_1- & T_2-MR imaging experiments were performed on a Siemens Prisma 3.0T MR scanner (Erlangen, Germany), and the pulse sequence used was a T_1-weighted imaging followed by T_2-weighted imaging. T_1 images were acquired with the following parameters—TR = 482 ms, TE = 16 ms: FOV: 40 × 90 cm; matrix: 208 × 256; slice thickness = 1 mm, while T_2-weighted images were obtained with the following parameters—TR = 4800 ms, TE = 54 ms: FOV: 40 × 90 cm; matrix: 208 × 256; slice thickness = 1 mm; coil: volume.

PA imaging was performed on a MSOT imaging system (128 inVision, iThera Medical, Germany). Images were acquired with an 808 nm pulsed laser excitation. After acquiring the imaging data, the images were reconstructed using a model-based algorithm provided in the View MSOT software suite.

Photothermal therapy and distribution study

After mice were anaesthetised, 5 mg kg^{-1} of MGNs–FA solution was injection through the tail vein, every other day, for PTT therapy. Thermal images were captured using a thermo camera (Thermo Gear G100, NEC, Japan) to measure temperature increase and depth of heat penetration, while tumour location was illuminated by the 808 nm continuous wave laser at 1.0 W cm^{-2} for 10 min after MGNs–FA injection. During the next 14 days, all mice were sacrificed and potential acute cytotoxicity and biodistribution in major organs (tumour, heart, lungs, liver, spleen, and kidneys) were assessed by haematoxylin and eosin (H&E) staining.

Statistical analysis

Mean values, standard deviations, and *p*-values were calculated in Microsoft Excel 2016. All error bars represent the standard deviations. The data were analyzed using a one-way ANOVA statistical analysis and indicated with *p*-values for significance; *p*-values of <0.05 were considered to be statistically significant.

Results and discussion

Synthesis and characterisation of MGNs–FA

As shown in Fig. 1, functional MGNs–FA nanoparticles contain three crucial components, namely, small size, tumour targeting ligand and functionality. (1) Some reports have claimed that nanoparticles with sizes ranging between 10–100 nm are optimal for enhanced permeability and retention and for evading the reticuloendothelial system (RES) in the liver and the spleen.[4,25,26] (2) Folic acid was used as a targeting ligand for HCC theranostics[10,27] and surface modification with folic acid–PEG derivative (SH–PEG–FA) can result in greater tumour targeting and biocompatibility. (3) The magneto-gold theranostic nanoagent, which acts as both a photothermal agent and T_1- & T_2-MRI/CT/PAI quad-modality imaging contrast agent, can provide complementary information for early and accurate cancer diagnosis and real-time therapeutic monitoring.

The magneto-gold nanoparticles (Fe_3O_4–Au, MGNs) were prepared using a modified coprecipitation method reported in our previous work.[4] The ultra-small Fe_3O_4 nanoparticle cores were firstly synthesized, then the MGNs were formed by the reduction of $HAuCl_4$ onto the surfaces of Fe_3O_4 with poly(acrylic acid) as a seeding agent and $NaBH_4$ as a reducing agent at low temperature. Transmission electron microscopy (TEM) images revealed that the MGNs were 7 nm ± 0.5 nm diameter in size with a monodisperse spherical shape, as shown in Fig. 2a. TEM images acquired after surface modification with SH–PEG–FA, which was based on high affinity connections of gold–thiol interaction,[28] showed that the MGNs–FA had an obvious core–shell structure of around 25 nm diameter (Fig. 2b). Hydrodynamic diameter distribution (Fig. 2c) revealed that average MGNs–FA diameter was 50.4 nm, that the MGNs–FA remained homogenous for 14 days at 4 °C, and that they were well-dispersed without need for sonication. These observations indicate that the MGNs–FA are small-sized and do not aggregate in aqueous solutions, and that they can evade the reticuloendothelial system (RES), to persist in circulation for an adequate period of time to show good lesion accumulation rate.[29,30]

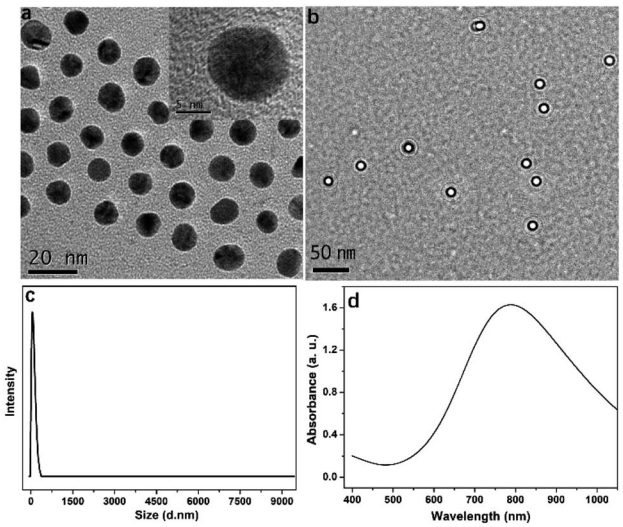

Fig. 2 Characterization: TEM and HR-TEM (inset) images of MGNs (a). TEM images of MGNs–FA (b). Hydrodynamic diameter of the MGNs–FA aqueous solution at 200 μg mL^{-1} (c). UV-Vis-NIR absorption spectrum of MGNs–FA at 200 μg mL^{-1} (d).

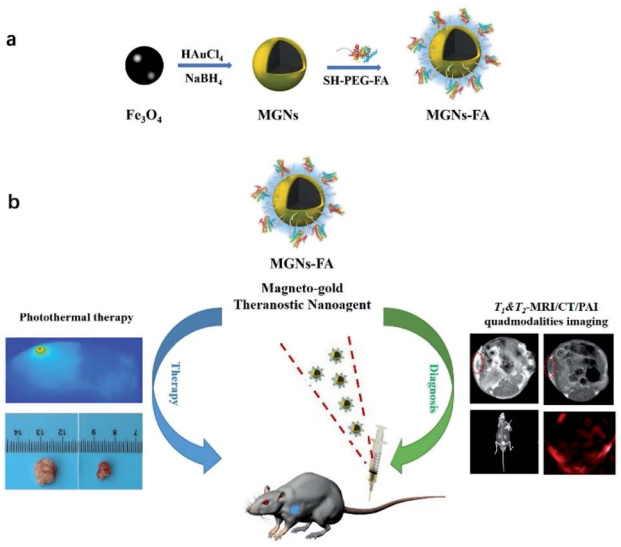

Fig. 1 A schematic diagram of synthetic route toward MGNs–FA (a) and as theranostic nanoagent (MGNs–FA) used for T_1- & T_2-MRI/CT/PAI (quad-modality) imaging and PTT therapy of tumour-bearing mice (b), wherein the PEG derivative was used for biocompatible encapsulation and folic acid enhanced tumour targeting.

The UV-Vis-NIR absorption spectrum (Fig. 2d) showed that the MGNs–FA solution has an obvious broad absorption in the visible range with a NIR window at around 800 nm, which corresponds to the wavelength required for maximum tissue penetration.[28] Significantly, spectral data also indicate that MGNs–FA can be used as a photothermal agent to efficiently convert NIR light to heat for photothermal therapy. Finally, inductively-coupled plasma mass spectrometry (ICP-MS) analysis revealed that the weight percentage of Fe and Au encapsulated in MGNs–FA was 15.4% and 19.9%, respectively.

In vitro T_1- & T_2-MRI/CT/PAI quad modalities imaging

The multimodality images of MGNs–FA at various concentrations in PBS solution were acquired. CT imaging ability of the MGNs–FA was assessed by acquiring CT phantom images and analysing Hounsfield unit (HU) values of synthesised MGNs–FA at various weight concentrations (0–500 μg mL; Fig. 3a). The results showed dose-dependent and positive contrast enhancement as the concentration of MGNs–FA increased, indicating that MGNs–FA nanoagents display high contrast efficacy during CT imaging.

Next, we investigated contrast characteristics during PA imaging using different concentrations (Fig. 3b) and found that PA images of the samples were much brighter as the concentration increased, suggesting that PA signal intensity was also dependent on the concentration of MGNs–FA used.

Both T_1- & T_2-weighted MRI imaging characteristics of MGNs–FA were evaluated by measuring their longitudinal and

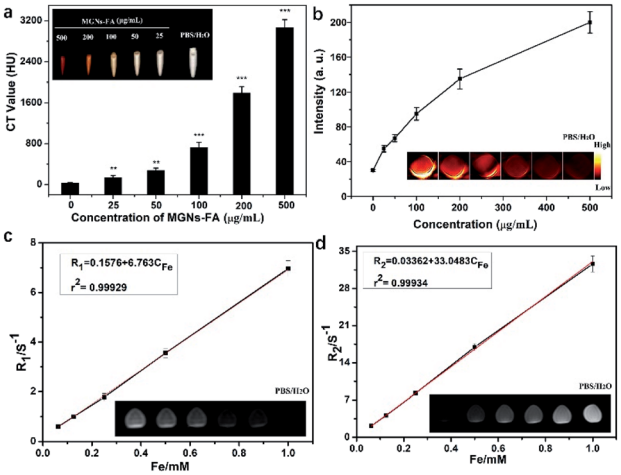

Fig. 3 Quad modalities imaging *in vitro*. Standard curve of HU values and CT phantom images of MGNs–FA at various concentrations (0–500 μg mL^{-1}) (a). Standard curve of PA signal values and PA images of MGNs–FA at various concentrations (0–500 μg mL^{-1}) (b). Plot of $1/T_1$ and $1/T_2$ over MGNs–FA and T_1- & T_2-MRI images of MGNs–FA at various Fe concentration (0.0625, 0.125, 0.25, 0.5, 1 mM and PBS solution) (c and d).

transverse relaxation rates (r_1 and r_2) at various concentrations in aqueous solution. As shown in Fig. 3c and d, MGNs–FA exhibit a relatively high r_1 value of 6.763 mM^{-1} s^{-1} and a common r_2 value of 33.048 mM^{-1} s^{-1}. As reported previously,[31] compared to large-sized Fe_3O_4 nanoparticles which only serve as T_2-negative CA, the ultra-small size of the Fe_3O_4 used inside the MGNs–FA enabled both T_1- & T_2-weighted MRI. Further, as the size shrinks, magnetisation of the nanoparticle tends to dramatically decrease due to the lack of complete spin alignment in the atoms on the surface. This property accounts for the MGNs–FA exhibiting lower r_2 relaxivity to compared to larger-sized particles (*e.g.* SHU-555C, $r_2 = 69$ mM^{-1} s^{-1}). While attributable to low magnetic moment, weaker susceptibility effect and the large surface area to small size ratio, MGNs–FA exhibited higher r_1 values than those of commercial T_1-positive CA, such as Gd–DTPA ($r_1 = 4.8$ mM^{-1} s^{-1}). The corresponding T_1- & T_2-weighted MR images of MGNs–FA nanoparticles at different concentrations are provided as insets in Fig. 3b and c, and it is obvious from the data that MR signal intensity is gradually enhanced with increasing the concentration of MGNs–FA, implying that MGNs–FA could provide superior sensitivity when used as a contrast agent during T_1- & T_2-weighted MRI.

Photothermal effect and photostability of MGNs–FA

As shown in the UV-Vis-NIR absorption spectrum, MGNs–FA exhibited an intense and broad absorption band in the visible region, along with a strong and broad NIR absorption peak around at 800 nm; the latter endows MGNs–FA with potential for use in photothermal therapy with NIR laser irradiation. Upon laser exposure (808 nm, 1.0 W cm^{-2}), the temperature of MGNs–FA at various concentrations increased in an apparent concentration-dependent or irradiation duration-dependent

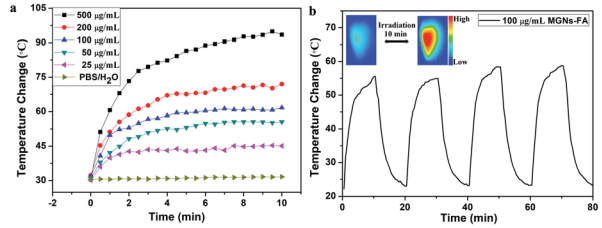

Fig. 4 Temperature changes in MGNs–FA solutions at various concentrations upon 808 nm laser irradiation for 10 min (a). Photothermal stability study and infrared thermal imaging (insert) of MGNs–FA dispersion (100 μg mL^{-1}) upon laser irradiation (b).

manner (Fig. 4a). In comparison, under identical conditions, there was negligible rise in temperature in the PBS/H_2O sample used as control. Temperature elevation in the MGNs–FA solutions at concentrations as low as 100 μg mL^{-1} could be easily increased from 25 °C to 55.6 °C with 10 min of continuous laser irradiation. The infrared thermal imaging camera utilised to monitor real-time temperature of MGNs–FA at 100 μg mL^{-1} (inset, Fig. 4b), showed that temperatures were high enough to cause thermal ablation of the tumour.[2,32] Furthermore, photothermal stability of MGNs–FA upon laser irradiation (Fig. 4b) remained unaltered after four cycles, suggesting that MGNs–FA had excellent photothermal stability.

Cytotoxicity assay *in vitro*

An excellent theranostic nanoagent should exhibit good biocompatibility; thus, the MTT assay was used to test the cytotoxicity of the MGNs–FA. The results showed that MGNs–FA had low cytotoxicity as cell viability was above 92.0% (Fig. 5a) even at a high concentration of 500 μg mL^{-1}, probably because of modification with an excellent biocompatible PEG derivative. At the same time, hemocompatibility test was also performed to investigate the safety of the MGNs–FA towards red blood cells, the results (Fig. S1†) show synthesized MGNs–FA have almost negligible damage to the red blood cells (<5% hemolytic activity).

Additionally, the LDH assay was used to evaluate damage to the cell membrane due to MGNs–FA as LDH is released through the damaged cell membrane.[33] The LDH content of the supernatant of cells exposed to various concentrations of MGNs–FA for 24 h showed that the LDH level was slightly higher in MGNs–FA-incubated cells than unexposed control cells, but only at

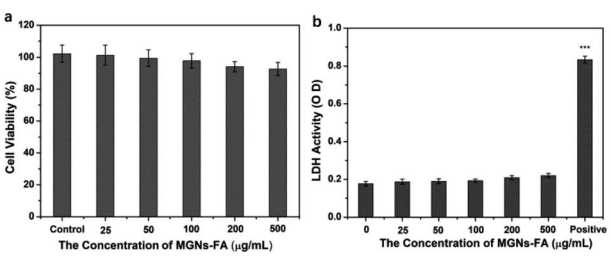

Fig. 5 Cell viability (a) and LDH assay (b) in HUVECs cells incubated with various concentrations of MGNs–FA for 24 h, ***$p < 0.001$.

a concentration of 100 μg mL^{-1} (Fig. 5b). Notably, even at MGNs–FA concentration of 500 μg mL^{-1}, the LDH value was significantly lower than that of the positive control (H_2O_2). Importantly, these results are consistent with those obtained with the MTT assay and confirm biocompatibility of the MGNs–FA.

Cellular studies

Targeting capability of MGNs–FA to cancer cells overexpressing the folate receptor was studied using SMMC-7721 cells, and to prove clear tumour targeting using imaging, Cy5 was used to label the surface of the MGNs–FA. Cy5-labelled MGNs without FA were used as controls. Fig. 6a shows confocal images of SMMC-7721 cells after incubation with 100 μg mL^{-1} Cy5-labelled MGNs–FA or Cy5-labelled MGNs for one hour, respectively. The results clearly show greater internalisation of the Cy5-labelled MGNs–FA into cells compared to Cy5-labelled MGNs (Fig. 6a), indicating that more MGNs–FA were internalised into tumour cells *via* folate receptor-mediated endocytosis. The results are further confirmed by average fluorescence intensity measured by flow cytometry (Fig. S2†). This indicates that, as a specific target protein, FA can significantly enhance the tumour targeting and cellular uptake. Thus, these results confirm that MGNs–FA can be effectively used for targeting folate receptor expressing cancer cells.

To test cellular PTT potential of MGNs–FA, NIR laser irradiation (808 nm) was applied to SMMC-7721 cells incubated with 100 μg mL^{-1} MGNs–FA. Live/dead cells immunofluorescence (calcein-AM/PI) co-staining, wherein green fluorescence due to calcein-AM indicates live cells and red fluorescence due to PI staining indicates dead cells, showed that the strongest red colour was seen in the treatment combination of MGNs–FA + NIR laser irradiation (Fig. 6b), and that it was higher than that of any other monotherapy group. This observation suggests the NIR irradiation or nanoagent alone did not result in tumour cell death, and that, notably, MGNs–FA are promising PTT agents.

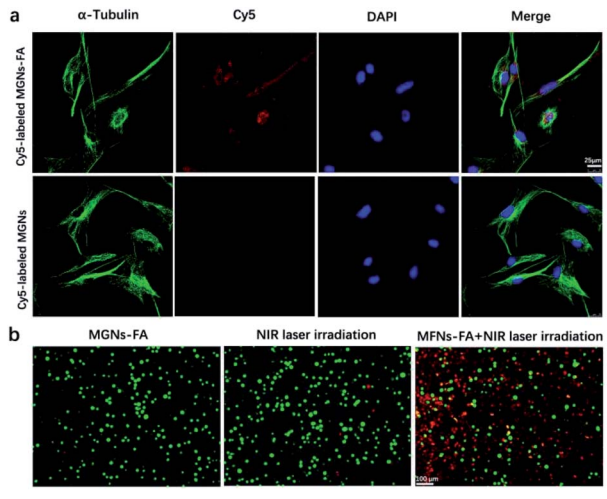

Fig. 6 Confocal images of SMMC-7721 cells after uptake of Cy5-labelled MGNs–FA or Cy5-labelled MGNs (a), scale bars are 25 μm. The SMMC-7721 cellular PTT of MGNs–FA: fluorescence microscopy images of live and dead cell staining, green fluorescence represents living cells and red fluorescence represents dead cells. The scale bars are 100 μm (b).

T_1- & T_2-MRI/CT/PAI quad modalities imaging *in vivo*

MRI is a non-invasive imaging technique and a powerful tool for detecting both tumours and therapeutic response. MGNs–FA with higher r_1 and r_2 relaxivity are also expected to simultaneously enhance both T_1- and T_2-weighted MR images and improve MRI sensitivity during early diagnosis of a tumour. Given the results of the *in vitro* contrast efficacy studies, we evaluated the *in vivo* contrast enhancing effect of MGNs–FA. MR imaging in a 3T MRI scanner was performed in tumour-bearing mice before and at 12 h after injection of a solution of MGNs–FA. Representative T_1 and T_2 MR images are shown in Fig. 7a, and compared to images before injection, significant contrast enhancement in the tumour was observed at 12 h post-injection. Specifically, on T_1-weighted MRI, the signal was enhanced and the tumour appears brighter, while on T_2-weighted MRI, the signal is reduced and the tumour is darker. These results indicate that MGNs–FA have excellent HCC cancer targeting properties and could be used as promising CA for simultaneous T_1- & T_2-MRI applications.

Next, we evaluated *in vivo* tumour CT imaging capabilities of MGNs–FA (Fig. 7b) and show that the bright signal of the tumour can be seen promptly and clearly after MGNs–FA injection and that CT values in Hounsfield units (HU) for the tumours increased from 125 HU before MGNs–FA injection to 1520 HU after injection. Thus, as expected, MGNs–FA can be used as a contrast agent for *in vivo* tumour CT imaging.

For *in vivo* PA imaging, sensitivity and deep tissue penetration were also evaluated, and MSOT analysis was performed before and after MGNs–FA injection into tumour-bearing mice. We found that PAI signals indicating the tumour location in mice increased dramatically at 12 h post-injection (Fig. 7c).

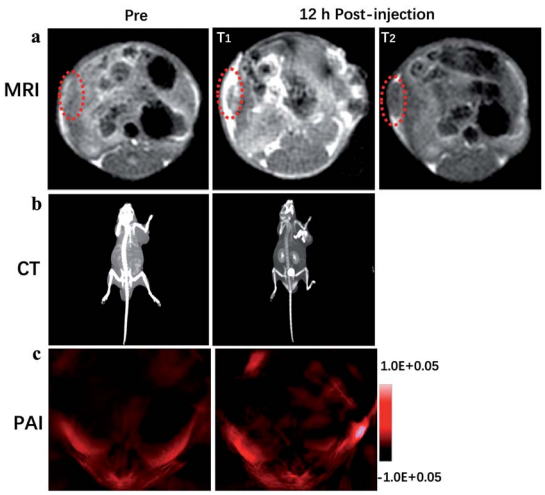

Fig. 7 *In vivo* quad-modality tumour imaging with T_1- & T_2-MRI/CT/PAI in tumour-bearing mice, before and at 12 h after injection with MGNs–FA.

Specifically, these signals at 12 h were 5.1 times greater than those obtained before injection, implying authentic accumulation of MGNs–FA in the tumour tissue and indicating usefulness of MGNs–FA as a contrast agent for *in vivo* PAI.

Photothermal therapy *in vivo*

Cellular studies *in vitro* had revealed good antitumor efficacy of MGNs–FA when used as a PTT agent. To investigate the photothermal performance of MGNs–FA *in vivo*, a series of studies on antitumor effectiveness were conducted. When tumour volume in mice reached a range of ~500 mm^3, 5 mg kg^{-1} of MGNs–FA solution was injected every other day and mice were subjected to NIR light radiation (808 nm, 1.0 W cm^{-2}) for 10 min at 12 h after injection. PBS (pH = 7.4) was intravenously injected into mice used as control animals. Thermal images were captured during irradiation to measure temperature increase and depth of heat penetration, and as seen in Fig. 8a, temperature in the tumour quickly (within 10 min) increased to 55 °C in the nanoagent-injected group, which is considered sufficient for thermal ablation of tumours. In contrast, the control group showed only negligible temperature rise. Further, changes in tumour volume were also calculated to evaluate direct therapeutic effects, and the tumour volume change during 14 days of PTT therapy was shown in the Fig. S3.† All the mice were sacrificed after seven injections and the tumour tissues were excised, photographed (Fig. 8b) and measured (Fig. 8c). Compared to controls, the therapy group showed remarkable tumour shrinkage (73.72 ± 4.28% reduction in weight) even though body weight (Fig. 8d) of the mice remained stable or showed slight increase during the same period. Collectively, these results suggest that heat generated by MGNs–FA upon NIR laser irradiation can effectively ablate tumours with no systemic side effects. Additionally, an essential feature of MGNs–FA is their biocompatibility *in vitro* and *in vivo* and H&E staining analysis (Fig. 8e) of the main organs showed no obvious morphological changes or injuries, indicating no appreciable *in vivo* toxicity.

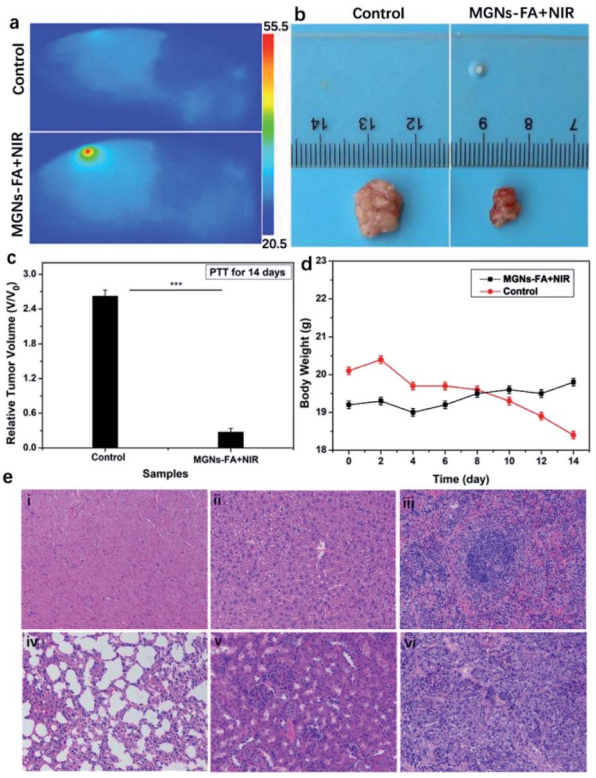

Fig. 8 NIR thermal therapy imaging of tumour-bearing mice intravenously injected with PBS or MGNs–FA and subjected to 808 nm laser irradiation (1 W cm^{-2}) for 10 min (a). Representative photographs of the tumours excised after 14 days of PTT treatment (b). Relative tumour volume of control and treated groups (c) and changes in body weight during PTT (d). H&E staining of main organs ((i) heart, (ii) liver, (iii) spleen, (iv) lung, (v) kidney and (vi) tumour) obtained from mice after PTT treatments (e).

Conclusions

To summarise, we describe the synthesis and characterisation of a novel multifunctional MGNs–FA that can be used as theranostic nanoagent due to its tumour targeting properties and suitability for multimodal imaging-guided PTT. This nanoagent integrates ultra-small MGNs and surface modifications that permit tumour targeting, enhance colloidal and photothermal stability and enable excellent *in vitro* and *in vivo* biocompatibility—these characteristics expected in moieties that can be used for T_1- & T_2-MRI/CT/PAI quad-modality imaging with high photothermal antitumor efficacy. Notably, the results of *in vivo* mouse experiments after treatment with photothermal therapy indicate that MGNs–FA are highly effective and safe as theranostic nanoagents. Therefore, these MGNs–FA have great potential in T_1- & T_2-MRI/CT/PA imaging guided therapy because they incorporate characteristics that permit both PTT and comprehensive imaging for diagnosis.

Author contributions

GW conceived and designed the study. JL and DW performed the experiments. JL provided the *in vivo* imaging and edited the manuscript. All authors read and approved the final manuscript.

Conflicts of interest

There are no conflicts to declare.

Acknowledgements

We gratefully acknowledge support by Liaoning Revitalization Talents Program of China (No. XLYC1807037).

References

1 G. Yu, S. Yu, M. L. Saha, J. Zhou, T. R. Cook, B. C. Yung, J. Chen, Z. Mao, F. Zhang, Z. Zhou, Y. Liu, L. Shao, S. Wang, C. Gao, F. Huang, P. J. Stang and X. Chen, *Nat. Commun.*, 2018, **9**, 4335.

2 D. Yan, X. Liu, G. Deng, H. Yuan, Q. Wang, L. Zhang and J. Lu, *J. Colloid Interface Sci.*, 2018, **530**, 547–555.
3 S. Yang, Q. You, L. Yang, P. Li, Q. Lu, S. Wang, F. Tan, Y. Ji and N. Li, *ACS Appl. Mater. Interfaces*, 2019, **11**, 6777–6788.
4 G. N. Wang, K. Qian and X. F. Mei, *Nanoscale*, 2018, **10**, 10467–10478.
5 X. Li, L. Xing, K. Zheng, P. Wei, L. Du, M. Shen and X. Shi, *ACS Appl. Mater. Interfaces*, 2017, **9**, 5817–5827.
6 C. Wu, R. Zhang, W. Du, L. Cheng and G. Liang, *Nano Lett.*, 2018, **18**, 7749–7754.
7 S. Zhao, R. Tian, B. Shao, Y. Feng, S. Yuan, L. Dong, L. Zhang, K. Liu, Z. Wang and H. You, *ACS Appl. Mater. Interfaces*, 2019, **11**, 394–402.
8 T. Kim, Q. Zhang, J. Li, L. Zhang and J. V. Jokerst, *ACS Nano*, 2018, **12**, 5615–5625.
9 X. Li, C. Schumann, H. A. Albarqi, C. J. Lee, A. W. G. Alani, S. Bracha, M. Milovancev, O. Taratula and O. Taratula, *Theranostics*, 2018, **8**, 767–784.
10 Z. Wang, D. Shao, Z. Chang, M. Lu, Y. Wang, J. Yue, D. Yang, M. Li, Q. Xu and W. Dong, *ACS Nano*, 2017, **11**, 12732–12741.
11 L. Gao, J. Yu, Y. Liu, J. Zhou, L. Sun, J. Wang, J. Zhu, H. Peng, W. Lu, L. Yu, Z. Yan and Y. Wang, *Theranostics*, 2018, **8**, 92–108.
12 L. Guang, F. Zhang, F. Yu, W. J. Sun, M. Song, X. Chen, X. Z. Zhang and X. L. Song, *Biomaterials*, 2017, **129**, 28–36.
13 W. Fan, B. Yung, P. Huang and X. Chen, *Chem. Rev.*, 2017, **117**, 13566–13638.
14 S. M. Dadfar, K. Roemhild, N. I. Drude, S. Stillfried, R. Knüchel, F. Kiessling and T. Lammers, *Adv. Drug Delivery Rev.*, 2019, **138**, 302–325.
15 L. Tang, F. Zhang, F. Yu, W. Sun, M. Song, X. Chen, X. Zhang and X. Sun, *Biomaterials*, 2017, **129**, 28–36.
16 P. Das, P. Fatehbasharzad, M. Colombo, L. Fiandra and D. Prosperi, *Trends Biotechnol.*, 2019, **37**, 995–1010.
17 C. Yin, G. Wen, C. Liu, B. Yang, S. Lin, J. Huang, P. Zhao, S. H. D. Wong, K. Zhang, X. Chen, G. Li, X. Jiang, J. Huang, K. Pu, L. Wang and L. Bian, *ACS Nano*, 2018, **12**, 12201–12211.
18 G. Chen, H. Qiu, P. N. Prasad and X. Chen, *Chem. Rev.*, 2014, **114**, 5161–5214.
19 M. D. Yang, C. H. Hcka, O. Hovorka, F. R. Chen, P. S. Lai and C. H. Lai, *Adv. Mater.*, 2018, **30**, 1802444.
20 R. Jin, L. Liu, W. Zhu, D. Li, L. Yang, J. Duan, Z. Cai, Y. Nie, Y. Zhang, Q. Gong, B. Song, L. Wen, J. M. Anderson and H. Ai, *Biomaterials*, 2019, **203**, 23–30.
21 M. Sun, L. Xu, W. Ma, X. Wu, H. Kuang, L. Wang and C. Xu, *Adv. Mater.*, 2016, **28**, 898–904.
22 Y. Liu, Z. Yang, X. Huang, G. Yu, S. Wang, Z. Zhou, Z. Shen, W. Fan, Y. Liu, M. Davisson, H. Kalish, G. Niu, Z. Nie and X. Chen, *ACS Nano*, 2018, **12**, 8129–8137.
23 W. Dong, Y. Li, D. Niu, Z. Ma, J. Gu, Y. Chen, W. Zhao, X. Liu, C. Liu and J. Shi, *Adv. Mater.*, 2011, **23**, 5392–5397.
24 J. Huang, M. Guo, H. Ke, C. Zong, B. Ren, G. Liu, H. Shen, Y. Ma, X. Wang, H. Zhang, Z. Deng, H. Chen and Z. Zhang, *Adv. Mater.*, 2015, **27**, 5049–5056.
25 A. Albanese, P. S. Tang and W. C. W. Chan, *Annu. Rev. Biomed. Eng.*, 2012, **14**, 1.
26 G. N. Wang, X. J. Zhang, Y. X. Liu, Z. J. Hu, X. F. Mei and K. Uvdal, *J. Mater. Chem. B*, 2015, **3**, 3072–3080.
27 D. Shao, J. Li, Y. Pan, X. Zhang, X. Zheng, Z. Wang, M. Zhang, H. Zhang and L. Chen, *Biomater. Sci.*, 2015, **3**, 833–841.
28 C. Li, T. Chen, I. Ocsoy, G. Zhu, E. Yasun, M. You, C. Wu, J. Zheng, E. Song, C. Z. Huang and W. Tan, *Adv. Funct. Mater.*, 2014, **24**, 1772–1780.
29 G. N. Wang, W. Gao, X. J. Zhang and X. F. Mei, *Sci. Rep.*, 2016, **6**, 28258.
30 F. Bao, J. L. Yao and R. A. Gu, *Langmuir*, 2009, **25**, 10782–10787.
31 G. N. Wang, X. J. Zhang, Y. X. Liu, A. Skallberg, Z. J. Hu, X. F. Mei and K. Uvdal, *Nanoscale*, 2014, **6**, 2953–2963.
32 X. Liu, Y. Wang, Q. Yu, G. Deng, Q. Wang, X. Ma, Q. Wang and J. Lu, *Colloids Surf., B*, 2018, **166**, 161–169.
33 Y. Gao, J. Kang, Z. Lei, X. F. Mei and G. N. Wang, *Nanoscale Res. Lett.*, 2020, **15**, 53.